PCCP

Accepted Manuscript

ROYAL SOCIETY OF CHEMISTRY

www.rsc.org/pccp

Dye Sensitized Solar Cell from Polyaniline-ZnS Nanotubes and its Characterization through Impedance Spectroscopy

Arnab Shit, Shreyam Chatterjee, and Arun K. Nandi*

Polymer Science unit, Indian Association for the Cultivation of Science,

Jadavpur, Kolkata- 700032, India

• For Correspondence: A. K. Nandi email: psuakn@iacs.res.in

Abstract:

Polyaniline (PANI) - zinc sulphide (ZnS) nanocomposites (PAZs) are synthesized by polymerizing aniline in presence of acetic acid taking different concentrations of ZnS nanoparticles (NPs). FESEM and TEM images indicate nanotube morphology of PANI and ZnS NPs remain adhered at the nanotube surface, but at higher ZnS concentration the nanotube morphology is lost. UV-Vis spectra indicate PANI in the doped state and the doping increases with increase of ZnS concentration. Fluorescence intensity passes through a minimum with ZnS content and the dc-conductivity of the composites gradually increase with increase in ZnS NP concentration. The I-V plot of PAZ composites indicates that the photocurrent is higher than that of the dark current at each voltage and the device exhibits reversible turn ‘‘on’’ and ‘‘off’’ by switching ‘‘on’’ and ‘‘off’’ the white light illumination. Dye sensitized solar cells fabricated with PAZ composites indicate a reasonably higher power conversion efficiency (η = 3.38%) than that of pure ZnS NPs. Attempt is made to shed light on the operating mechanism of the DSSC from the impedance data using Cole - Cole plot by drawing an equivalent circuit illustrating the different electronic and ionic transport processes within the cell.

Keywords: Non-covalent interaction, photoluminescence, dc-coductivity, photocurrent, Cole-Cole plot

Introduction:

Recently dye-sensitized solar cells (DSSCs) have turned up as the most promising systems to accomplish efficient solar-energy conversion as they are inexpensive, flexible and easier to fabricate than silicon solar cells. [1-3] TiO_2 nanostructures[1,4-6] have been studied extensively as the photoelectrode material in DSSC and the record of high power conversion efficiency of DSSC has continued for nearly two decades.[7] Further increase in the power conversion efficiency (PCE) has been restricted by energy loss due to recombination between electrons and either the oxidized dye molecules or electron-accepting materials in the electrolyte during the charge transport course.[1,8-10] In TiO_2 based DSSCs the TiO_2 layers are the key parameters through which the generated photoelectrons at the dye molecules transport to the anode. During this process a reverse charge transfer from TiO_2 to the I_3^-/I^- redox couple or to the dye may occur causing reduction in the PCE. Such a recombination problem is more prominent for TiO_2 nanocrystals due to the deficiency of depletion layer on the TiO_2 nanocrystallite surface and becomes more severe when the photoelectrode film thickness is increased.[1] So alternative materials are necessary in place of TiO_2 to obtain a maximum PCE. Different 1D nanostructures such as nanotubes,[1,11] nanowires,[1,2,12,13] nanosheets,[14,15] and nanobelts[16] have been employed as functional nanostructured photoelectrodes to enhance the electron diffusion length in the photoelectrode films as they provide a direct conduction pathway for the rapid collection of photogenerated electrons. Nanostructures with different semiconductor other than TiO_2, are particularly desirable to further increase the interest in DSSC so as to improve it's PCE.

Conducting polymers have attracted considerable attention because of their unique properties, such as reversible convertibility between redox states, metallic conductivity, fast charge/discharge capacities, high charge transport rates and short diffusion distances for ion transport.[17] Similarly different shapes and size controlled inorganic semiconductor synthesis

has also occupied a vital part of materials research[18-21] as they have potential applications in different areas.[21-24] The fabrication of hybrid nanocomposites by assembling the organic and inorganic precursors at the molecular level by controlling the morphology, interfaces and structure is a challenging task. Such hybrid materials look promising and are gaining attention because the synergism between the components often gives rise to properties that are superior to the sum of the individual constituents. Harnessing the benefits of both the constituents requires excellent tuning of the spatial assembly of individual domains and their interfaces. [25,26]

In search of the alternative of TiO_2, these types of above said organic-inorganic hybrids may be useful. Already different semiconductor oxides, such as ZnO, SnO_2, or Nb_2O_5 are employed as the photoelectrode to fabricate DSSC.[27,28] But sulphide based metal semiconductor as an photoelectrode, alternate to TiO_2 in DSSC, is scared in literature. A reverse charge transfer in the DSSCs (recombination reaction) from TiO_2 to the dye or to the redox couple may be reduced by incorporating conductive network into the semiconductors.[29-31] Hence we have used a newly *in-situ* synthesized nanotube morphology of polyaniline (PANI)- zinc sulphide (ZnS) hybrid to fabricate the DSSC, as the ZnS is attached to a highly conducting PANI polymer network.

Usually, AC impedance spectroscopy is used as a non-destructive testing tool for the study of electrolytic materials[32-35] and the impedance diagrams are generally interpreted from equivalent circuit models which can give insight into the microstructural features of the material. Presently, the mechanism of solar cell operation is understood by Cole-Cole plot of impedance values, measured at the open circuit voltage of the cell.[36-39] In the impedance analysis a small AC voltage amplitude exerts a very small perturbation shedding light on the salient ionic and electronic process inside the DSSC.

Here, we report the synthesis of nanotube morphology of PANI-ZnS composite by the *in - situ* polymerization of aniline in the presence of ZnS NPs. The new type of nanotubular PANI-ZnS composites are used to fabricate a DSSC with N719 dye (cis-di (thiocyanate)bis-(2,2′-bipyridyl-4,4′-dicarboxylate)-ruthium(II) (bis tetrabutylammonium) as a photosensitizer. The drastic enhancement in the PCE is observed with different content of ZnS in the composite. The highest PCE upto 3.38% is obtained from the composites. To our knowledge this is the highest PCE obtained using ZnS polymer composite to date. Probable mechanism for the nanotube morphology of the composite and the higher power conversion efficiencies of the systems are discussed accordingly. Attempt has been made to elucidate the conduction mechanism of photoelectrons in DSSC from Cole-Cole (Nyquist) plot of the cell obtained from impedance spectroscopy.

Experimental:

Materials:

Acetic acid, zinc acetate, sodium sulphide, ammonium persulphate (APS), aniline were purchased from E. Merck, Mumbai are used as received except aniline. Middle fraction of distilled aniline is used for polymerization in this work.

Synthesis of PANI-ZnS nanocomposites:

ZnS nanoparticles are synthesized by wet chemical method using zinc acetate ($Zn(Ac)_2 \cdot 2H_2O$) and sodium sulphide (Na_2S) precursors (details in SI). The PANI-ZnS composites are synthesized by polymerization of aniline (182 µL) in the presence of a different concentrations of ZnS (25, 50, 100, 250, 400 and 500 mg) dispersion and the composites such produced are designated as PAZ1, PAZ2, PAZ3, PAZ4, PAZ5 and PAZ6, respectively. In a typical procedure, ZnS nano particles are added into 5 mL of 0.2 (M) acetic acid solution, and the mixture is ultrasonicated until ZnS is fully dispersed (1 h). Then 182

μL aniline is added into the above solution and is stirred for 30 min at 20°C to form a uniform mixture. 11.42 gm APS, is dissolved in 100 ml 0.2 (M) acetic acid solution and is cooled at 20°C. The polymerization is performed by rapid addition of 5 ml APS solution to the above monomer solution at 5°C and the mixture is aged for self assembly for 24 h at 5°C. The product is dried at 60°C for 24 h under vacuum. The yields of pure PANI, PAZ1 and PAZ4 composites are found to be 81.5, 81.1 and 79% (W/W) respectively.

Characterization:

The powder samples are spread on carbon tape and are platinum coated for surface morphology and field emission scanning electron microscope (FE-SEM) images are recorded from a JEOL, JSM-6700F FE-SEM instrument. The morphology of the samples is also studied under transmission electron microscope (TEM) in a JEOL, 2010 EX instrument operated at a voltage of 200 kV. Dilute aqueous dispersion of the sample is dropped on a carbon coated copper grid and after drying it is directly observed through the TEM. The tube diameters are measured for thirty places from the TEM micrographs and average values with standard deviations are presented. The FTIR spectra of the samples are taken from the KBr pellets of the samples in a Shimadzu FTIR instrument (model 8400S). UV-Vis spectra of the samples are taken from water solution (0.2mg/mL) using a UV-Vis spectrometer (model 8453, Hewlett-Packard). The solutions are prepared by sonicating the samples in water and the spectra are recorded by taking them in a quartz cell of 1 mm path length. The photoluminescence (PL) spectra are recorded from aqueous dispersion of the pure and composite in 1 cm quartz cell in FluoroMax-3 (Horiba-Jobin Yvon) instrument. Wide angle X-ray scattering (WAXS) patterns of dried samples are recorded using a Bruker AXS diffractomer (model D8 Advance) fitted with a Lynx Eye detector. The instrument is operated at 40 kV voltage and 40 mA current. The samples are scanned from 2θ = 15-60° at the scan rate of 0.5 s/step with a step width of 0.02°. The dc-conductivity is measured by two-probe

method by sandwiching the sample between two indium-titanium oxide (ITO) conducting strips of 1 mm width placed perpendicularly. The area of the sample was 0.01 cm^2 and the thickness of the samples is measured by a digital slide calipers. The dc-conductivity of the sandwiched samples is measured by an electrometer (Keithley, model 617) at 30°C using the equation:

$$\sigma = \frac{1}{R} \times \frac{l}{a}$$

where '*l*' is the thickness and 'a' is the area and 'R' is the resistance of the sample. The I-V characteristics curves of the samples are studied at 25 ^oC using the same samples by applying voltage from -5 to +5 V and the current is measured at each applied voltage. Electrochemical impedance measurements are performed with a Solartron SI1260 impedance analyzer. The impedance spectra are recorded at a frequency range of 1Hz to 1MHz with an oscillation voltage of 100mV at an applied DC voltage of 0.78V, i.e at the open circuit voltage of the cell.

Dye Sensitized Solar Cell Fabrication:

The substrates (pure ZnS and PANI-ZnS composites) are sensitized by immersing them into 0.5 mM ethanolic solution of the N719 dye for approximately 20 min. The sensitization time is firmly controlled to avoid the dissolution of surface Zn atoms and the formation of Zn^{2+}/dye complexes, which may block the electron transport from the dye to the active material. The samples are then carefully rinsed with ethanol to remove the additional dye. The photoelectrodes are fabricated on low resistance ITO glass (2x2cm^2, 8-12Ω) by drop-cast method. A thin layer of graphite is coated on the ITO using a pencil tip which acts as the counter electrode. The iodide-triiodide based electrolyte solution, consisting of 0.5 M KI, 0.05 M I_2 in γ-butyrolactone, is placed on the active electrode area. The average active

electrode area is around 0.68 cm^2. The electrodes are separated by a 60-μm parafilm strip and are sandwiched together with clips. A small space of bare ITO glass is uncovered for wire connection on the anode. Platinum is typically used to catalyze the triiodide reduction reaction, but for the high cost and lack of availability it is not compatible with an inexpensive sustainable technology. Thus it is an advantage of our system to use the low cost graphite material counter electrode to get a reasonable PCE. The configuration of the solar cell is achieved by putting the samples opposite to the ITO substrate on the top of the counter electrode in face-to-face fashion, respectively, to prepare the DSSCs with pure ZnS and PANI-ZnS composites. The cell current between the two electrodes is measured using a Keithley source meter (model 2401) by illuminating under AM1.5G light illumination of 100 mW cm^{-2} from a 150 W Xenon lamp source (Newport Corp. USA; model no. 67005).

Results and Discussion:

Morphology:

In Fig. 1 and in Fig.S1 the FESEM images of the ZnS NPs, pure PANI, and the four PANI-ZnS nanocomposites (PAZ1, PAZ2, PAZ3 and PAZ4) are presented. Pure ZnS has a nanosphere morphology and the pure PANI formed in the acetic acid medium exhibits the nanotube morphology. After in situ polymerization in presence of ZnS NPs, the composites retain the nanotube morphology of the PANI along with the ZnS NPs adhering to the surface. However, at higher concentration of ZnS NPs some clusters of ZnS NPs are also noticed on the surface PANI nanotube. The TEM images in Fig.2 and in Fig. S2 also exhibit the nanotubular morphology of the PAZ1-PAZ4 composites, distinctly. The average nanotube diameters of the composites are measured to be 127±2, 134±2, 150±3, 171±2, 199±5 nm for PANI, PAZ1, PAZ2, PAZ3 and PAZ4, respectively and the increase may be attributed to the adhering of more ZnS NPs on the surface of PANI nanotube. The EDAX spectra of PAZ3

and PAZ4 samples (Fig. S3 and S4) characterize the presence of zinc, carbon, nitrogen and sulphur atoms suggesting the presence of both ZnS and PANI in the sample.

The mechanism of the formation of PANI nanotubes in the acetic acid medium has been explained by Stejskal et al.[40] The aniline oligomers (phenazine) are produced in solution at the initial stage of aniline oxidation, and act as a template for the adsorption of *N*-phenylphenazines produced during the induction period. The vesicle template for the growth of nanotubes is thus produced by the stacking of the short *N*-phenylphenazines around the phenazine nanocrystallites.[29] Subsequently the stacked *N*-phenylphenazines initiation centers facilitate the PANI chains to grow producing the supramolecular vesicles thus producing the walls of nanotubes. The ZnS NPs then become adhered to the surface of PANI nanotube through supramolecular interaction, the nature of which will be delineated through FTIR spectroscopy. In PAZ5 and PAZ6 the nanotube morphology is lost possibly due to the hindrance of vesicle template formation required for the formation of the PANI nanotubes by the large concentration of ZnS NPs. It might be also possible that for higher ZnS concentration a large portion of APS is consumed in reaction with ZnS forming $ZnSO_4$ even in the mild acidic condition. This may result in a deficiency of APS concentration to polymerise aniline into sufficient amount of PANI changing its tubular morphology.

Spectroscopy:

FTIR Spectra:

Fig. 3 presents the FTIR spectra of the pure PANI, ZnS NPs, and PANI–ZnS nanocomposites (PAZ1, PAZ2, PZ3 and PAZ4) to verify the formation of PANI and its interaction with ZnS in the composites. The presence of stretching bands at 1579, 1493, 1297, 1139 and 799 cm^{-1} reveal the formation of PANI. The characteristic stretching vibrations at 1579-1586 cm^{-1} arises mainly from both C=N and C=C stretching of the quinonoid (Q) structure and the vibration band at 1493-1498 cm^{-1} is attributed to the aromatic ring stretching of the benzenoid

(B) structure of doped PANI. The peak at 1297-1299 cm^{-1} characterizes the stretching band for C–N vibration of the secondary aromatic amine and the band at ~1139-1144 cm^{-1} arises due to polaron formation on doping of PANI (Q=N^{+}H-B or B-N^{+}H-B).[41] In ZnS the peak at 1624 cm^{-1} is due to adsorbed CO_2 on ZnS surface.[42] The C-H aromatic in-plane bending vibration occurs at the region 1040-1043 cm^{-1} and the out of plane deformation occurs at 799-818 cm^{-1} supporting the formation of PANI-ZnS composites.[43,44] These characteristic bands confirm that the PANI remains as conducting emeraldine salt (ES) phase.

The spectra for the PANI-ZnS nanocomposites show some shifts in the vibrational bands compared to those of pure PANI. As for example, both the benzonoid and quinonoid ring vibrations are shifted to higher energy indicating some interaction between ZnS and the electron clouds of the PANI rings. The shifting to higher energy indicates the localization of electron clouds of both the benzonoid and quinonoid rings probably due to the partial transfer of nonbonding electrons from sulphur of ZnS to the PANI chain that acts as an acceptor. This causes electron clouds of the benzonoid and quinonoid rings to become somewhat more localized causing difficulty in the ring vibration, shifting the vibration to higher frequency. This may be reasonable to consider that sulphur atom in ZnS is electron rich as Zn has filled d-orbitals. Therefore, partial transfer of nonbonding electrons of sulphur to the PANI chain may occur. So a donor acceptor type non-bonding interaction exists in PANI- ZnS nanocomposites and it increases with increase in ZnS Np concentration in the composite. It is to be noted here that the –C-H out of plane vibration of the benzene ring shows a substantial shift from 799 to 818 cm^{-1} with increase of ZnS concentration and may be attributed to the closely packed ZnS nanoparticles on the PANI chains prohibiting the out of plane deformation vibration significantly. The –C-H in plane stretching vibration of aromatic ring, however, shifts to a lower extent (1040 - 1043 cm^{-1}), also indicating some hindrance experienced from the ZnS adhering on PANI nanotube.

UV-Vis Spectra:

In Fig. 4 the UV-vis spectra of PANI, ZnS NPs and all the composites are presented. In pure PANI, the absorption peaks at 357, 438 and 873 nm correspond to π– π*, polaron band to π* band and π band to localized polaron band transitions of PANI (ES), respectively.[45,46] The absorption peak at 321 nm corresponds to the ZnS NPs[47] but in the case of the composites the peak due to ZnS is not prominent for the formation of the composite. The tail of the localised polaron band of PANI is broad and it becomes more broadened with increasing ZnS concentration in the composite suggesting better delocalization of the polarons with increasing ZnS concentration.

A quantitative analysis of the UV-Vis spectra indicate that both the polaron band to π* band and π band to localized polaron band transitions of PANI (ES) exhibit red shifts of 8-9 nm and the π– π* absorption peak exhibits a somewhat lower red shift of 3 nm. The red shifts suggest a decrease of the respective band gap energy (Scheme-1) and the reduction of π– π* transition band may be attributed to the increase of electron density in the benzonoid and quinonoid ring due to partial transfer from sulphur atom of ZnS. The red shift in polaron band transitions may be understood from the schematic band diagram (Scheme-1) where the shift of π– and π* bands to the localized polaron band causes the red shifts of both the transitions. The reason of lowering of π* band with the addition of ZnS is unknown and may be attributed to the cluster formation of the charge carriers at its excited state.

Photoluminescence (PL) spectra:

The photoluminescence (PL) spectra of PANI and PANI-ZnS nanocomposites (PAZ1, PAZ2, PAZ3, PAZ4, PAZ5 and PAZ6) are compared in Fig.5. The emission peak of ZnS NPs is centred at 397 nm with a hump at 461 nm (inset of Fig.5) for excitation by a radiation of λ = 320 nm. The above emission bands may be assigned to the stoichiometric vacancies or interstitial impurities in the ZnS NPs.[48,49] PL-spectrum of acetic acid doped PANI nanotube

for excitation at 320 nm shows a peak at 457 nm with negligibly small intensity compared with that of the composites and it may be neglected for discussion in the PANI-ZnS composites. It is observed from the spectrum that the PL- intensity decreases with increase in ZnS NPs content and the PL intensity shows an interesting variation with ZnS content showing a minimum for the PAZ4 sample. A possible reason for the initial PL-quenching may be that the excitons of ZnS get an alternative path for decay through the PANI chains of the nanotubes and as soon as the nanotube structure breaks at PAZ5 and PAZ6 the quenching begins to be lower. The nanotubes have a regular arrangement of PANI chains through which the decay of excitons occur very rapidly, but on breaking of the nanotube morphology at PAZ5 and PAZ6, the irregular arrangement of PANI chains perturb the decay paths and therefore the emission intensity begins to increase. The light filtering effect of PANI for quenching of PL-emission of PANI-ZnS nanocomposites may also be another cause for the apparent PL- quenching for the PAZ1 to PAZ4 samples. It is interesting to note that a red shift of the emission peak is obtained, possibly due to decrease of the band gap. Anyway the PL-quenching is a good indication for the PAZ composites to exhibit photovoltaic properties and PAZ4 is expected to show better photovoltaic properties.

WAXS study:

The powder XRD spectra of pure PANI, pure ZnS and their composites are shown in Fig. 6. The XRD spectrum of pure PANI exhibits a broad reflection at a Bragg angle (2θ) value of 23.8° corresponding to (200) diffraction plane of PANI ES structure of acetic acid doped PANI.[50] The ZnS NPs show diffraction peaks at 2θ = 26.9°, 28.3°, 30.3°, 39.7°, 47.6°, 53.0°, 56.7° which are in good agreement with the standard values of ZnS reported in JCPDS (Joint Committee on Powder Diffraction Standards, Card no. 36-1450) and can be indexed as the hexagonal wurtzite structure with the lattice constants a = 3.816 Å and c = 6.253 Å.[51] However, in the XRD spectra of the composites we observe that at 25 mg concentration of

ZnS in PANI (PAZ1) intensity of XRD peak due to PANI has been reduced significantly and XRD pattern of ZnS starts dominating. It is interesting to note that on further increasing the concentration of ZnS to 250 mg (PAZ4) the diffraction peaks due to ZnS are only observed, even though the composite contains same amount of PANI and it may be attributed to the strong scattering power of ZnS crystals than that of PANI. All other samples (PAZ2 and PAZ3) with higher concentration of ZnS also show XRD patterns due to ZnS only and the peak positions of the composites becomes also shifted towards higher Bragg angle (Table-1). In the table the d_{hkl} values of all the PAZ composites are computed and it is apparent from the table that the d_{hkl} values have decreased in the PAZ composites with increase in ZnS concentration compared to that of pure ZnS and it may be attributed to the squeezing of ZnS unit cells in presence of PANI in the PAZ composites. No definite reason of this quenching of unit cell is known and one probable reason may be attributed to the interaction of ZnS NPs with the acceptor PANI via partial electron transfer from the nonbonding electrons of ZnS. This transfer causes the electron clouds of filled d-shell of Zn to be quenched through a dπ-pπ type interaction squeezing the unit cell. XRD study thus suggests that during the formation of PAZ composites PANI undergoes interfacial non-bonding interactions with the ZnS nano crystallites.

dc-conductivity measurement:

The dc-conductivities of the samples are presented in Table 2 and the conductivity of ZnS (2.0×10^{-8} S/cm) is three orders lower than that of pure PANI nanotubes (1.63×10^{-5} S/cm). The conductivity of the composites is also similar in order with that of pure PANI nanotubes, but its value gradually increases with increase in ZnS NP concentration, although the latter is more nonconducting than that of PANI. It may be reasonable to think that the small increase of conductivity may be attributed to the secondary doping of PANI by ZnS NPs[40] due to the electronic interaction between the PANI and ZnS NPs as discussed above. This secondary

doping gradually increase with increase in ZnS NPs in the composites and in the case of PAZ4, it appears to be maximum resulting the highest conductivity amongst all the samples. The PAZ5 and PAZ6 samples however exhibit lower conductivity probably due to the loss of the ordered nanotube morphology.

Photoelectrochemical Properties:

The photoresponse of PANI-ZnS nanocomposites with gold electrode has been examined from the I-V plot under dark and illumination condition with 1.5AM irradiation (Fig.S5). The I-V plot indicates that at each voltage the photocurrent is higher than that of the dark current particularly for PAZ2- PAZ4 samples. In both the conditions the semiconducting nature of the I-V curves is observed. On white light irradiation at a bias of 5 V the photocurrent growth (for 100 s) and decay (for 100 s) are recorded at a time gap of 1ms. Fig.7 exhibits several such photocurrent cycles indicating that for the sample PAZ4 the device can be reversibly turned ‘‘on’’ and ‘‘off’’ by switching the white light illumination on and off, respectively. The increase of current after white light irradiation is 0.15mA and the data is quite reproducible as observed from the different cycles. From the different cycles of photocurrent it is clear that after making composite with ZnS, PAZ4 produces a stable photocurrent in a reproducible way whereas for PAZ1, PAZ2 and PAZ3 the data are not quite reproducible (Fig.S6). After illumination with white light there may be some photo-degradation at lower ZnS concentration of the composites i.e., PAZ1, PAZ2 and PAZ3 creating hindrance in charge flow causing a small decrease in the current for every cycle. A probable reason may be the degree of coating on the outer surface of PANI nanotubes by ZnS; lower the concentration of ZnS higher is the vacant surface of PANI nanotube where light interact to degrade the PANI chains.

Dye Sensitized Solar Cell:

We have fabricated dye sensitized solar cells (DSSC) with the composites using N719 dye as a photosensitizer. A counter electrode was made by coating a thin layer of graphite on the ITO glass. After absorbing the white light by the N-719 dye, the photo excited electron enters into the conduction band of the composite and then it flows to the external circuit, from which it is re-injected into the counter-electrode. A reference DSSC with pure ZnS NPs is also constructed for comparison. The J–V characteristic curves of all the DSSCs are compared in Fig.8. Important parameters including power conversion efficiency (PCE), open-circuit voltage (V_{oc}), short-circuit current density (J_{sc}), and fill factor (FF) are summarized in Table 3. The results show that the PCE of DSSCs increase with the increase of ZnS concentration up to 250 mg and then it decreases with further ZnS incorporation. From the figure it is clear that the PAZ4 composite based DSSC shows the highest short circuit current (J_{sc}= 7.78 mA/cm^2) and highest open circuit voltage (V_{oc}= 0.78 V) with reasonably higher power conversion efficiency (η = 3.38%) compared to those of the pure ZnS NPs and other PAZ composite based DSSCs. The cell characteristics of pure ZNS based DSSC are: V_{oc} = 0.73 V, J_{sc} =5.15 mA cm^{-2}, fill factor (FF)= 0.42 and η = 1.59% and those of PANI based DSSC are V_{oc}= 0.43V, J_{sc}= 0.22 mA/cm^2, FF= 0.31,η= 0.029% (Fig.S7). So there is a considerable increase of PCE with increasing the ZnS concentration (Table 3) in the PAZ composites and better J_{sc} with the PAZ4 composite is due to the small internal resistance as evident from the dc conductivity measurement of PAZ samples (Table-2).[52] In the PAZ composites with increasing ZnS concentration could increase the charge recombination at photoelectrode because of the slower reduction rate on the counter electrode,[53] and the breaking of PANI network in the higher nanoparticle concentration cause a decrease of PCE. These results indicate that proper amount of ZnS nanoparticle incorporation into the PANI network can significantly improve the performance of PANI-ZnS composite based DSSC and here it is observed that PAZ4 is the sample showing

optimum photovoltaic properties. We have studied the durability of PAZ4 sample by aging at 40 ^{0} C and we observed an unchanged value of PCE till 18 hrs of aging and after that 20% decrease of PCE occurs after 48 hrs of aging (Fig. S8 and Table S1).

A schematic diagram (Scheme 2) shows the operational principle of the PANI-ZnS composite based DSSC under 1.5 AM illumination. The relative energy levels of p-type PANI and n-type ZnS (conduction band, CB, and valence band, VB) are shown. The LUMO of PANI (-2.14 eV)[54] receives electrons from the photo excited dye and the excited electrons can pass through the PANI tube to the conduction band of ZnS (-1.75 eV)[55] without any obstruction. Because the ZnS is adhered with the conducting PANI tube, the collected electrons can, therefore, transport from PANI to ZnS to ITO quickly (Scheme 2). The presence of conductive PANI nanotube onto the ZnS NPs may decrease the probability of recombination reaction. This is the probable reason to yield a reasonably higher short circuit current (J_{sc} = 7.78 mA/cm^2) than that of ZnS NPs based DSSC (J_{sc} = 5.15 mA/cm^2) as a reverse charge transfer in the DSSCs (recombination reaction) from ZnS to the dye or to the redox couple (I_3^-/I^-) may severely reduce the cell efficiency.[56] Thus the J_{sc} as well as the overall power conversion efficiency (η) is increased.[56] Also in all the PAZ1-4 samples, the nanotube morphology provides the high surface area which also helps the dye to be adsorbed very efficiently than that of PAZ5 and PAZ6 samples, causing a better power conversion efficiency.

Impedance Spectroscopy:

To understand the mechanism of photoelectron conduction within the photovoltaic cell we have recorded the impedance spectra on the application of open circuit voltage (0.78 V) for the PAZ4 sample. Fig. 9 shows a Cole- Cole plot of PAZ4 DSSC obtained from DSSC. Three semicircles are observed in the measured frequency range of 1-10^6 Hz. In our analysis, the three semicircles in the frequency region 10^5-10^6, 10^2-10^5, 1-10^2 Hz may be attributed to

three different charge transfer processes in the cell. In the high-frequency region, the first semicircular shape (Z1) may be assigned to impedances related to charge transport at the graphite counter electrode, in the middle-frequency region, the second semicircle (*Z*2) may correspond to that of the PAZ/dye/electrolyte interface and the low frequency region semicircular shape (*Z*3) corresponds to the iodine ion diffusion within the electrolyte, respectively. Each of the semicircles is analyzed from the Z-view software to obtain different resistance and capacitance values of the different parts DSSC. From the *Z*1, *Z*2, and *Z*3 semicircles the respective resistance of the PAZ/electrolyte interface (R_{rc}) and, the graphite/electrolyte interfacial resistance (R_g) and the iodine ion diffusion resistance (R_d) have been evaluated. The resistance elements R_{rc} , R_g , R_d , are estimated to be 1kΩ/cm^2, 0.2kΩ/cm^2 and 0.5kΩ/cm^2 respectively. The electron transport resistance of the working electrode to the counter electrode (R_s) which occurs at the very high frequency region (>10^6) could not be measured due to the limitation of the instrument. The capacitance of the elements Z1 (defined as capacitance of counter electrode/ electrolyte interface C_g), Z2 (defined as chemical capacitance C_μ), Z3 (iodine ion diffusion capacitance, C_D) are estimated to be 20nF, 5μF and 0.3 nF, respectively. The lifetime (τ) of photoelectrons can be measured using the formula

$$\tau = R_{rc} \times C_\mu$$

and the photoelectron lifetime is calculated to be 5 mili second. This lifetime value is 40-50 times lower than that of organic silane modified TiO_2 solar cell.[57] This indicates that photoelectrons undergo back reaction and recombination to a greater extent decreasing the cell efficiency.

From the above results we have drawn an equivalent circuit for the entire solar cell comprising of resistance and capacitance values of each process in the Fig. 10. The proposed

equivalent circuit is nearly similar to that of a conventional solar cell with an exception of having large values of capacitance. Since solar cell works under direct current condition so the effect of capacitance can be neglected during solar cell operation. Thus, this equivalent circuit may facilitate to get an insight into the operating mechanism of DSSC.

Conclusion:

The PAZ1, PAZ2, PAZ3, PAZ4 composites retain the nano-tubular morphology of PANI where ZnS NPs remain adhered to the nanotube surface of PANI but in PAZ5 and PAZ6 samples the nanotube morphology is lost possibly due to the hindrance of vesicle template formation required in the formation of nanotube by the large concentration of ZnS NPs. An interfacial non-bonding interaction exists between PANI and ZnS NPs in the nanocomposites through the sulphur atom of ZnS and doped PANI chain through a donor-acceptor type interaction and it increases with increase in ZnS NP concentration in the composite. The squeezing of ZnS unit cells in the PAZ composites is possibly due to the partial electron transfer from the nonbonding electrons of ZnS to PANI and it causes the electron clouds of filled d-shell of Zn to be quenched through a dπ-pπ type interaction. In PAZ4 sample the PL-intensity is minimum with a red shift of the emission peak suggesting the composite may exhibit good photovoltaic property. The doping of PANI increases with increase of ZnS concentration and the dc-conductivity of the composites gradually increases with increase in ZnS NP concentration due to secondary doping. At each voltage the PAZ composites exhibit higher photocurrent than dark current and the PAZ4 device exhibit reversibly turn ‘‘on’’ and ‘‘off’’ by switching “on” and “off” the white light illumination, respectively with an increase of 0.15 mA current after white light irradiation. Dye sensitized solar cells (DSSC) fabricated with the composites using N719 dye as a photosensitizer indicate that PAZ4 based DSSC shows the highest short circuit current (J_{sc}= 7.78 mA/cm^2) and highest fill factor (FF = 0.55) with reasonably higher power conversion efficiency (η = 3.38%) compared to those of pure

ZnS NPs and other PAZ composites. The operation of the DSSC has been understood from the cole - cole plot and equivalent circuit model characterizing the different electronic and ionic transport processes within the cell.

Acknowledgement:

We gratefully acknowledge CSIR (grant # 02 (0051)/12/EMR-II) for financial support. A. S. acknowledges DST-INSPIRE programme and S.C acknowledges CSIR, New Delhi for the fellowship.

Supporting Information:

FESEM & TEM, images and I-V curve, Photocurrent cycles of PANI-ZnS composites, DSSC of PANI and durability of PAZ4 DSSC. This information is available free of charge via the Internet at http://www.rsc.org/.

References:

1. B. Oregan, and M. Grätzel, *Nature,* 1991, **353**, 737-740.
2. Q. Zhang, C. S. Dandeneau, X. Zhou and G. Cao, *Adv. Mater.,* 2009, **21**, 1-22.
3. H. M. Cheng, W. H. Chiu, C. H. Lee, S. Y. Tsai and W. F. Hsieh, *J. Phys. Chem. C,* 2008, **112**, 16359-16364.
4. T. Ma, M. Akiyama, E. Abe and I. Imai, *Nano Lett.,* 2005, **5**, 2543-2547.
5. S. Guldin, S. Hüttner, M. Kolle, M. E. Welland, P. Müller-Buschbaum, R. H. Friend, U. Steiner and N. Tétreault, *Nano Lett.,* 2010, **10**, 2303-2309.
6. E. J. W. Crossland, M. Kamperman, M. Nedelcu, C. Ducati, U. Wiesner, D. -M. Smilgies, G. E. S. Toombes, M. A. Hillmyer, S. Ludwigs, U. Steiner and H. J. Snaith, *Nano Lett.,* 2009, **9**, 2807-2812.
7. Z. Yang, T. Xu, Y. Ito, U. Welp and W. K. Kwok, *J. Phys. Chem. C,* 2009, **113**, 20521-20526.
8. M. Grätzel, *Inorg. Chem.,* 2005, **44**, 6841-6851.
9. M. Grätzel, *J. Photochem. Photobiol. A,* 2004, **164**, 3-14.
10. J. Nissfolk, K. Fredin, A. Hagfeldt and G. Boschloo, *J. Phys. Chem. B,* 2006, **110**, 17715-17718.
11. A. B. F. Martinson, J. W. Elam, J. T. Hupp and M. J. Pellin, *Nano Lett.,* 2007, **7**, 2183-2187.
12. C. Y. Jiang, X. W. Sun, G. Q. Lo, D. L. Kwong and J. X. Wang, *Appl. Phys. Lett.,* 2007, **90**, 263501.
13. M. Law, L. E. Greene, J. C. Johnson, R. Saykally and P. Yang, *Nat. Mater.,* 2005, **4**, 455-459.
14. M. Fu, J. Zhou, Q. Xiao, B. Li, R. Zong, W. Chen and J. Zhang, *Adv. Mater.,* 2006, **18**, 1001-1004.

15. S. Kar, A. Dev and S. Chaudhuri, *J. Phys. Chem. B,* 2006, **110**, 17848- 17853.

16. X. Wang, Y. Ding, C. J. Summers and Z. L. Wang, *J. Phys. Chem. B,* 2004, **108**, 8773-8777.

17. S. I. Cho and S. B. Lee, *Acc. Chem. Res.,* 2008, **41**, 699-707.

18. J. S. Na, B. Gong, G. Scarel and G. N. Parsons, *ACS Nano.,* 2009, **3**, 3191-3199.

19. F. Dawood and R. E. Schaak, *J. Am. Chem. Soc.,* 2009, **131**, 424-425.

20. H. Zhao and E. P. Douglas, *Chem. Mater.,* 2002, **14**, 1418-1423.

21. J. Liu, T. Tanaka, K. Sivula, A. P. Alivisatos and J. M. J. Frechet, *J. Am. Chem. Soc.,* 2004, **126**, 6550-6551.

22. C. Yang, C. Xu and X. Wang, *Langmuir,* 2012, **28**, 4580-4585.

23. D. J. Gargas, H. Gao, H. Wang and P. Yang, *Nano Lett.,* 2011, **11**, 3792-3796.

24. K. T. Yong, H. Ding, I. Roy, W. C. Law, E. J. Bargey, A. Maitra and P. N. Prasad, *ACS Nano,* 2009, **3**, 502-510.

25. S. Chatterjee, A. Garai and A. K. Nandi, *Synth. Met.,* 2011,**161**, 62-71.

26. S. Chatterjee and A. K. Nandi, *Chem. Commun.,* 2011, **47**, 11510-11512.

27. K. Tennakone, G. R. R. A. Kumara, I. R. M. Kottegoda and V. P. S. Perera, *Chem. Commun.,* 1999, 15-16.

28. K. Sayama, H. Sugihara and H. Arakawa, *Chem. Mater.,* 1998, **10**, 3825-3832.

29. S. Chatterjee, R. K. Layek and A. K. Nandi, *Carbon,* 2013, **52**, 509-519.

30. S. Chatterjee, A. K. Patra, A. Bhaumik and A. K. Nandi, *Chem. Commun.,* 2013, **49**, 4646-4648.

31. S. Chatterjee, A. Shit and A. K. Nandi, *J. Mat. Chem. A,* 2013, **1**, 12302-12309.

32. J. R. Mcdonald, *Impedance Spectroscopy Emphasizing Solid Materials and Systems*, Wiley-Interscience, New York, 1987.

33. A. Karmakar and A. Ghosh, *Curr. Appl. Phys.,* 2012, **12**, 539-543.

34. F. B. Dias, L. Plomp and J. B. J. Veldhuis, *J. Power Sources,* 2000, **88,** 169-191.

35. P. Mukherjee, A. Kundu, S. Samanta, S. Roy and A. K. Nandi, *J. Phys. Chem. B,* 2013, **117**,1458-1466

36. L. Han, N. Koide, Y. Chiba and T. Mitate, *Appl. Phys. Lett.,* 2004**, 84,** 2433-2435.

37. Q. Wang, J. E. Moser and M. Grätzel, *J. Phys. Chem. B,* 2005, **109,** 14945-14953.

38. R. Kern, R. Sastrawan, J. Ferber, R. Stangl and J. Luther, *Electrochim. Acta.,* 2002**, 47**, 4213-4225.

39. J. van de Lagemaat, N. G. Park and A. J. Frank, *J. Phys. Chem. B*, 2000, **104,** 2044-2052.

40. J. Stejskal, I. Sapurina, M. Trchová and E. N. Konyushenko, *Macromolecules,* 2008, **41**, 3530-3536.

41. J. Stejskal, M. Trchová, J. Prokeš and I. Sapurina, *Chem. Mater.,* 2001, **13**, 4083-4086.

42. S. Ummartyotin, N. Bunnak, J. Juntaro, M. Sain and H. Manuspiya, *Solid State Sci.,* 2012, **14**, 299-304

43. T. Abdiryim, Z. Xiao-Gang and R. Jamal, *Mater. Chem. Phys.,* 2005, **90**, 367-372.

44. M. V. Kulkarni, A. K. Viswanath, R. Marimuthu and T. Seth, *J. Polym. Sci., Part A: Polym. Chem.,* 2004, **42**, 2043-2049.

45. Y. Xia, J. M. Wiesinger, A. G. MacDiarmid and A. J. Epstein, *Chem. Mater.,* 1995, **7,** 443-445.

46. J. Ruokolainen, H. Eerikäinen, M. Torkkeli, R. Serimaa, M. Jussila and O. Ikkala, *Macromolecules,* 2000, **33***,* 9272–9276.

47. M. J. Casciato, G. Levitin, D. W. Hess and M. A. Grover, *Ind. Eng. Chem. Res.,* 2012, **51**, 11710-11716.

48. S. Kar and S. Chaudhuri, *J. Phys. Chem. B,* 2005, **109***,* 3298-3302.

49. Q. Xiong, G. Chen, J. D. Acord, X. Liu, J. J. Zengel, H. R. Gutierrez, J. M. Redwing, L. C. L. Y. Voon, B. Lassen and P. C. Eklund, *Nano Lett.,* 2004, **4**, 1663-1668.

50. J. Joo, S. M. Long, J. P. Pouget, E. J. Oh, A. G. MacDiarmid and A. Epstein, *J. Phys. Rev. B,* 1998, **57**, 9567-9580.

51. S. Kar and S. Biswas, *ACS Appl. Mater. Interfaces,* 2009, **1**, 1420-1426

52. S. J. Peng, Y. Wu, P. Zhu, V. Thavasi, S. G. Mhaisalkar and S. Ramakrishna, *Photochem. Photobiol. A,* 2011, **223**, 97-102.

53. G. H. Guai, M. Y. Leiw, C. M. Ng and C. M. Li, *Adv. Energy Mater.,* 2012, **2**, 334-338.

54. T. Guo, L. Wang, D. G. Evans and W. Yang, *J. Phys. Chem. C,* 2010, **114**, 4765-4772.

55. A. L. Stroyuk, A. E. Raevskaya, A. V. Korzhak and S. Y. Kuchmii, *J. Nanopart. Res.,* 2007, **9**, 1027-1039.

56. A. Hagfeldt, G. Boschloo, L. Sun, L. Kloo and H. Pettersson, *Chem. Rev.,* 2010, **110**, 6595-6663.

57. G. A. Sewvandi, Z. Tao, T. Kusunose, Y. Tanaka, S. Nakanishi and Q. Feng, *ACS Appl. Mater. Interfaces,* 2014, **6**, 5818-5826.

Table 1: Comparison of d - spacing values (Å) of different PAZ composites

Sample	Amount of ZnS with 0.2mM Aniline	d_{100}	d_{002}	d_{001}	d_{102}	d_{110}	d_{103}	d_{112}
ZnS NPs	Pure ZnS	3.31	3.15	2.95	2.27	1.91	1.71	1.62
PAZ1	25 mg	3.19	3.05	2.87	2.27	1.93	1.76	1.67
PAZ2	50 mg	3.17	3.03	2.86	2.26	1.92	1.76	1.66
PAZ3	100 mg	3.15	3.02	2.84	2.25	1.92	1.78	1.66
PAZ4	250 mg	3.14	3.00	2.84	2.25	1.92	1.75	1.66
PAZ5	400 mg	3.13	3.00	2.83	2.25	1.91	1.75	1.66
PAZ6	500 mg	3.13	3.00	2.82	2.24	1.91	1.75	1.65

Table 2: dc-Conductivity values (S/cm) of different PAZ composites

Samples name	Conductivity value (S/cm)
ZnS	2.0×10^{-8}
PANI	1.6×10^{-5}
PAZ1	2.7×10^{-5}
PAZ2	3.2×10^{-5}
PAZ3	3.5×10^{-5}
PAZ4	4.3×10^{-5}
PAZ5	2.9×10^{-6}
PAZ6	3.3×10^{-6}

Table 3: Comparison of DSSC parameters made with ZnS and PAZ composites

Sample	Short Circuit Current, J_{sc} (mA/cm^2)	Open Circuit Voltage, V_{oc} (V)	Fill Factor, FF	Power Conversion Effeciency, η (%)
Pure ZnS	5.15	0.73	0.42	1.59
PAZ1	6.42	0.75	0.43	2.07
PAZ2	7.10	0.76	0.47	2.51
PAZ3	7.41	0.75	0.52	2.87
PAZ4	7.78	0.78	0.55	3.38
PAZ5	5.71	0.74	0.42	1.77
PAZ6	5.56	0.75	0.41	1.71

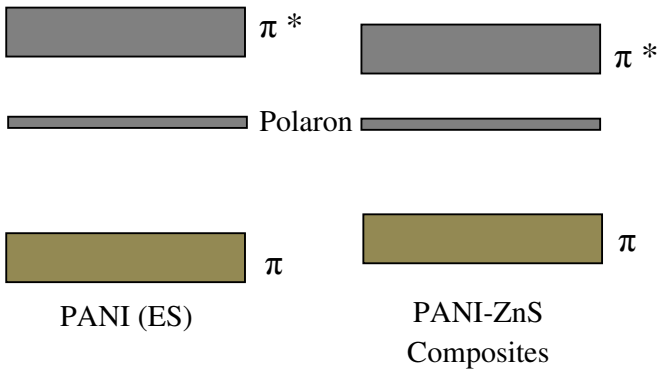

Scheme 1: Schematic band energy diagram of PANI (ES), and PANI-ZnS composites

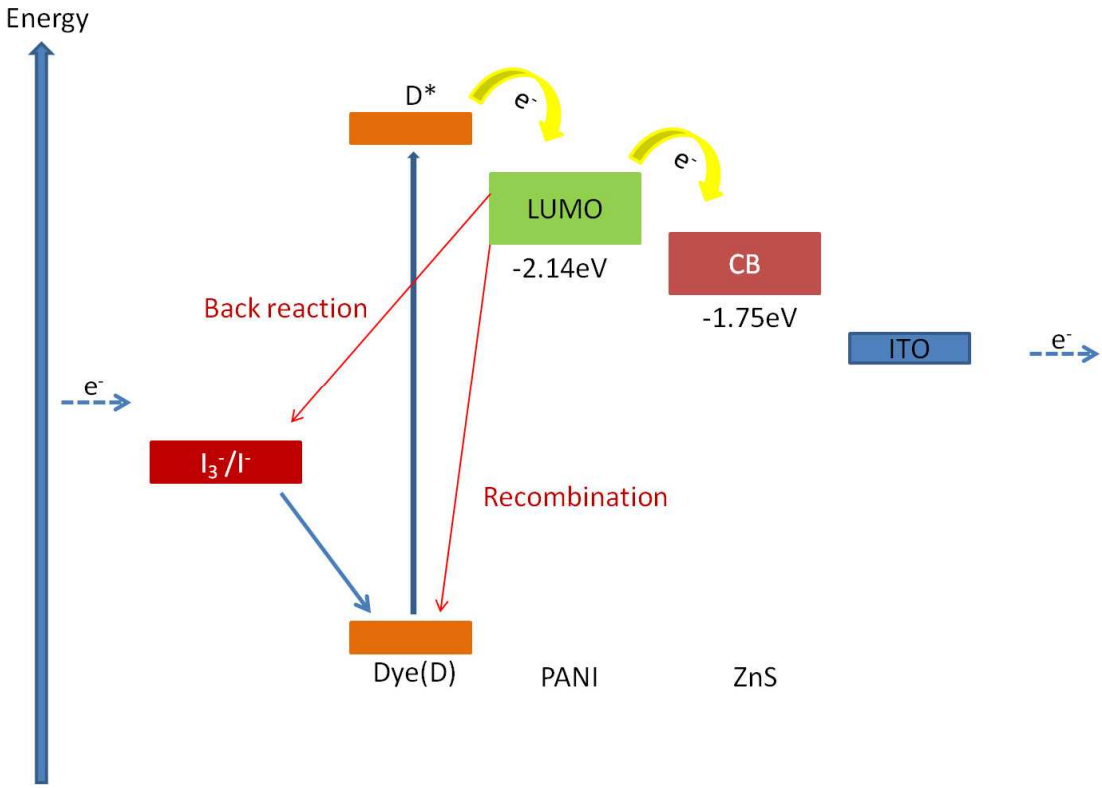

Scheme 2: Schematic model for the operation mechanism of the PANI-ZnS based DSSC

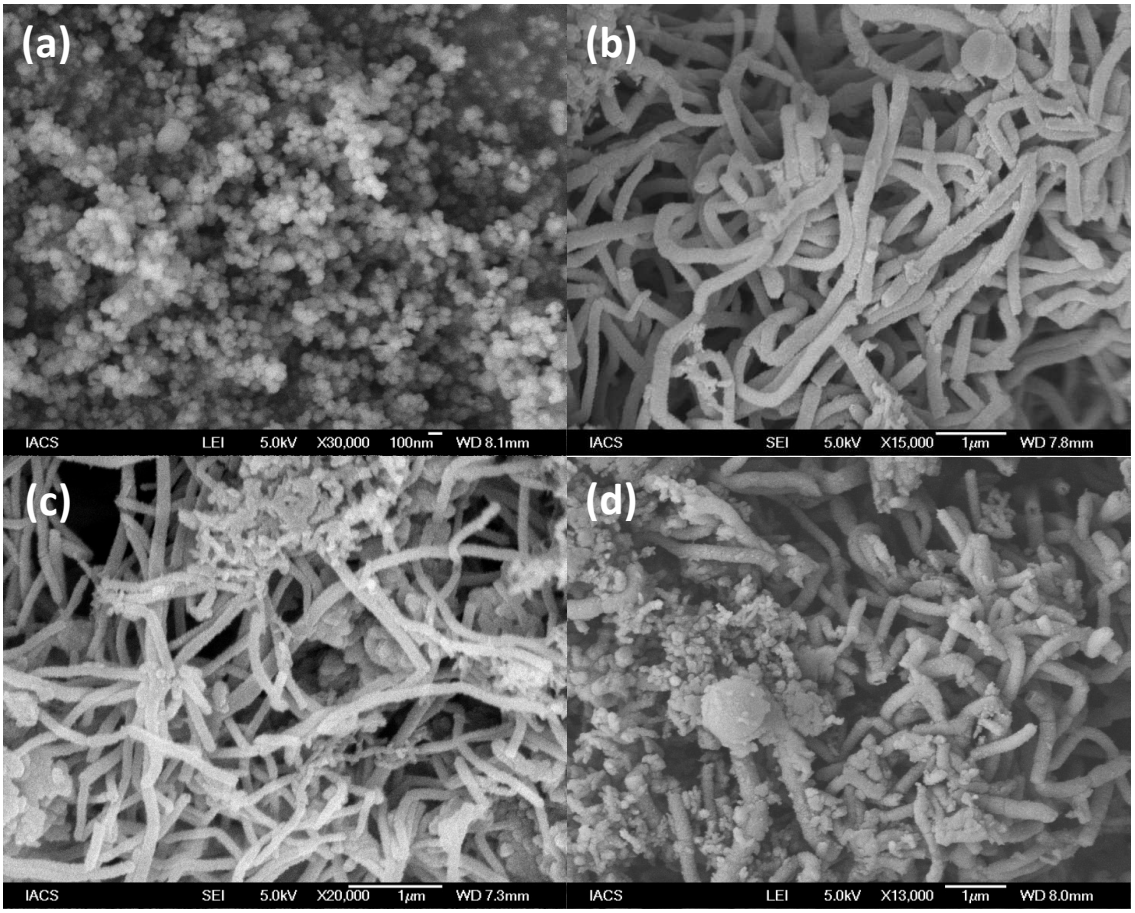

Fig. 1: FE-SEM Images of (a) ZnS NPs, (b) PAZ1, (C) PAZ3, (d) PAZ4

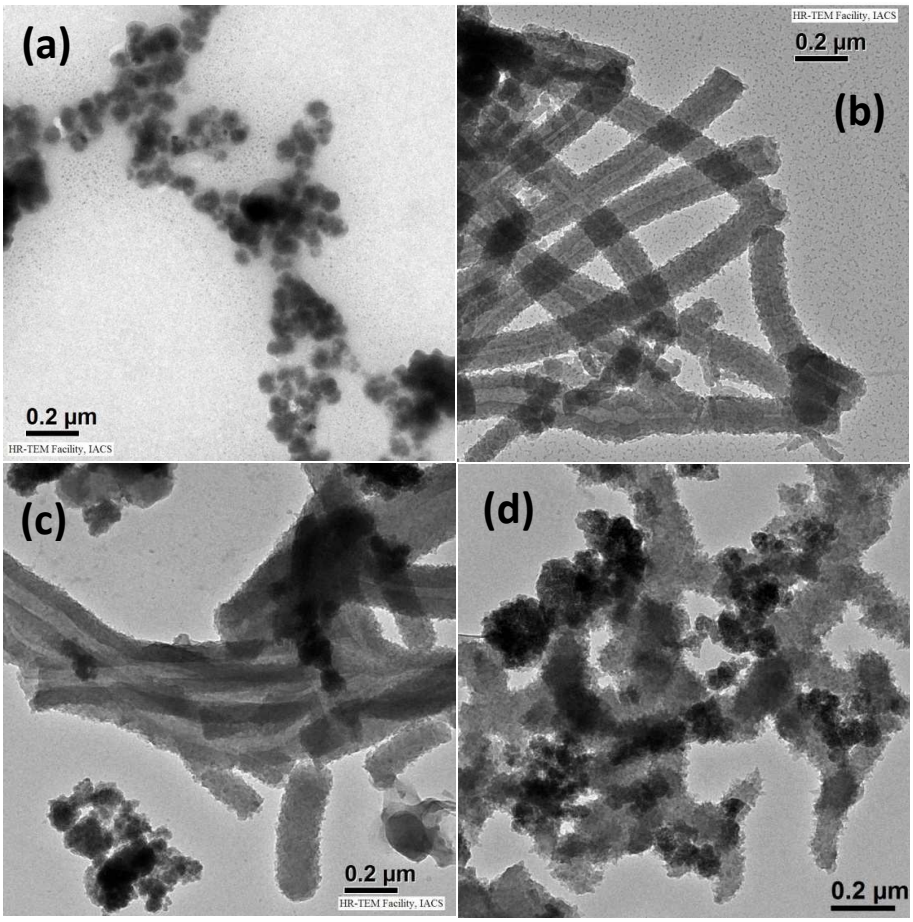

Fig. 2: TEM Images of (a) ZnS NPs, (b) PAZ3, (c) PAZ4, (d) PAZ5

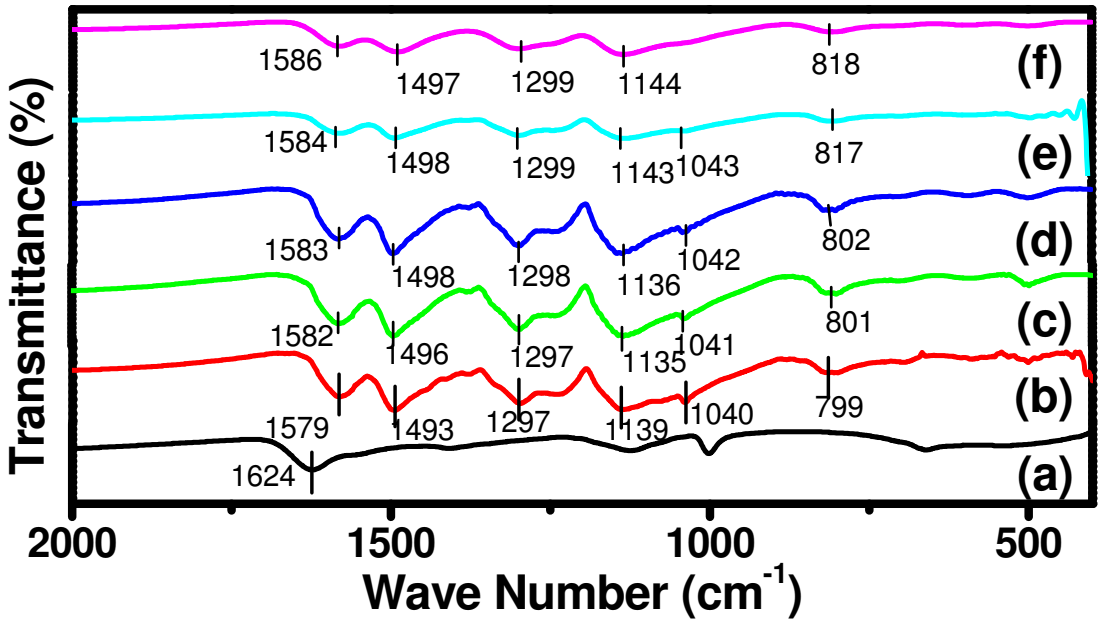

Fig. 3: FTIR Spectra of (a) Pure ZnS NPs, (b) PANI, (c) PAZ1, (d) PAZ2, (e) PAZ3, (f) PAZ4

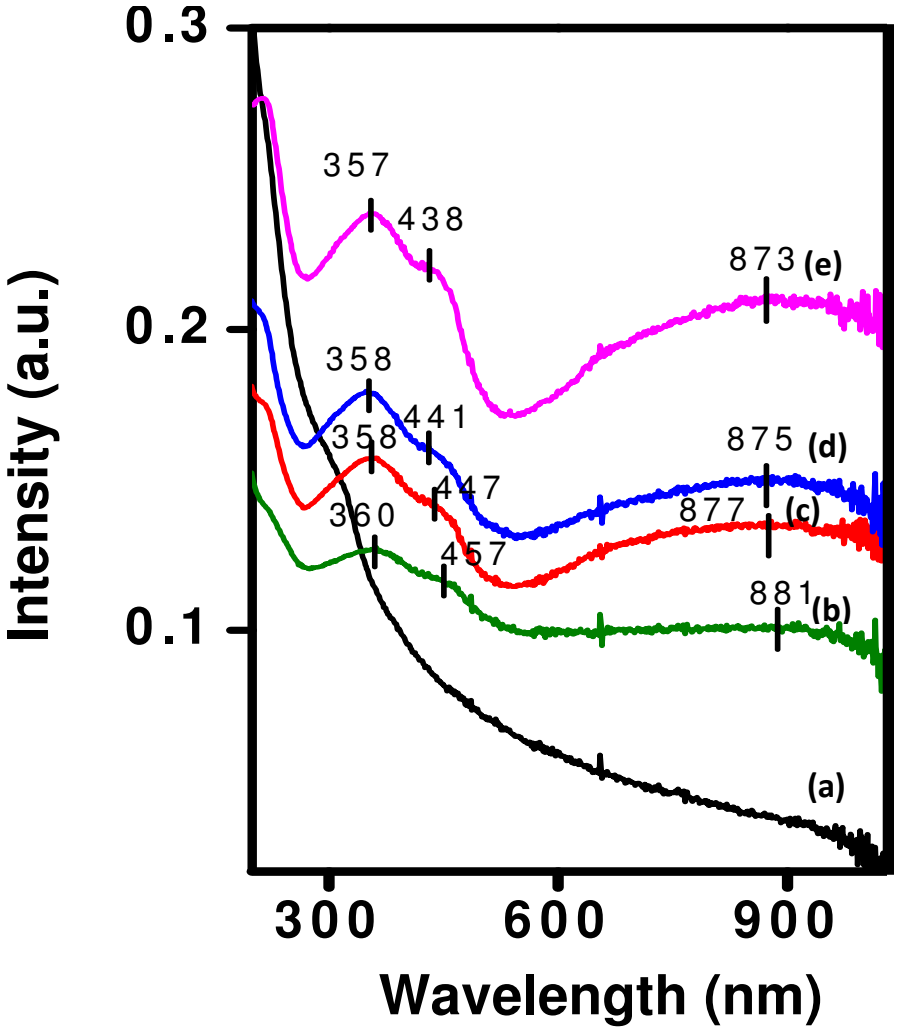

Fig. 4: UV-Vis Spectra of (a) Pure ZnS NPs, (b) PAZ6, (c) PAZ3, (d) PAZ1, (e) Pure PANI

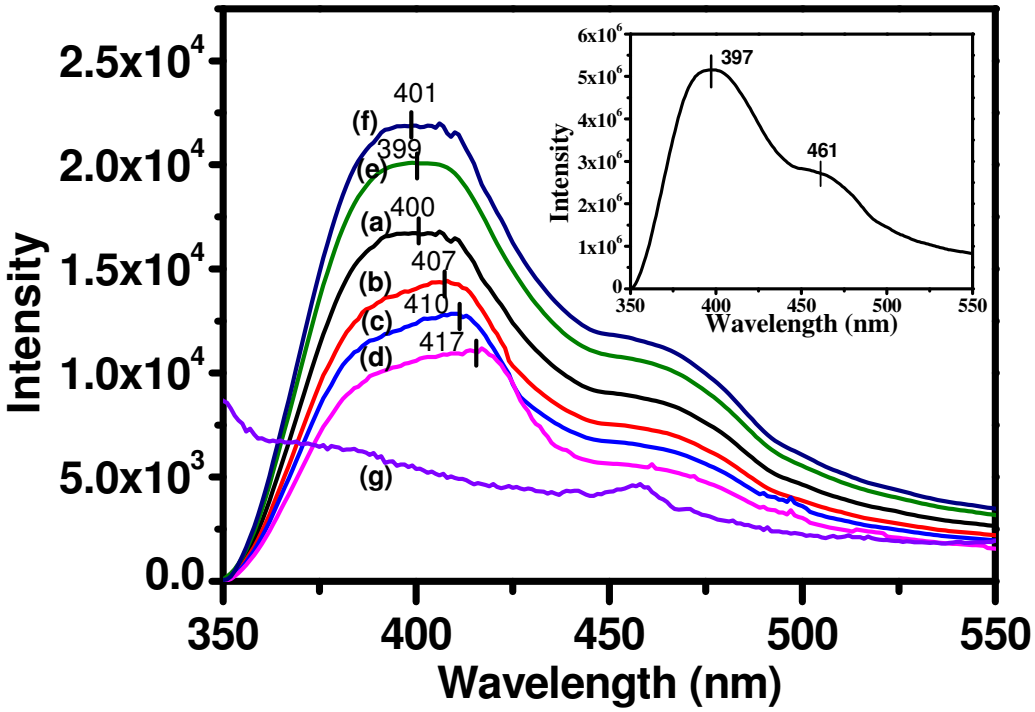

Fig. 5: PL Spectra of (a) PAZ1, (b) PAZ2, (c) PAZ3, (d) PAZ4, (e) PAZ5, (f) PAZ6, (g) Pure PANI Inset Pure ZnS NPs

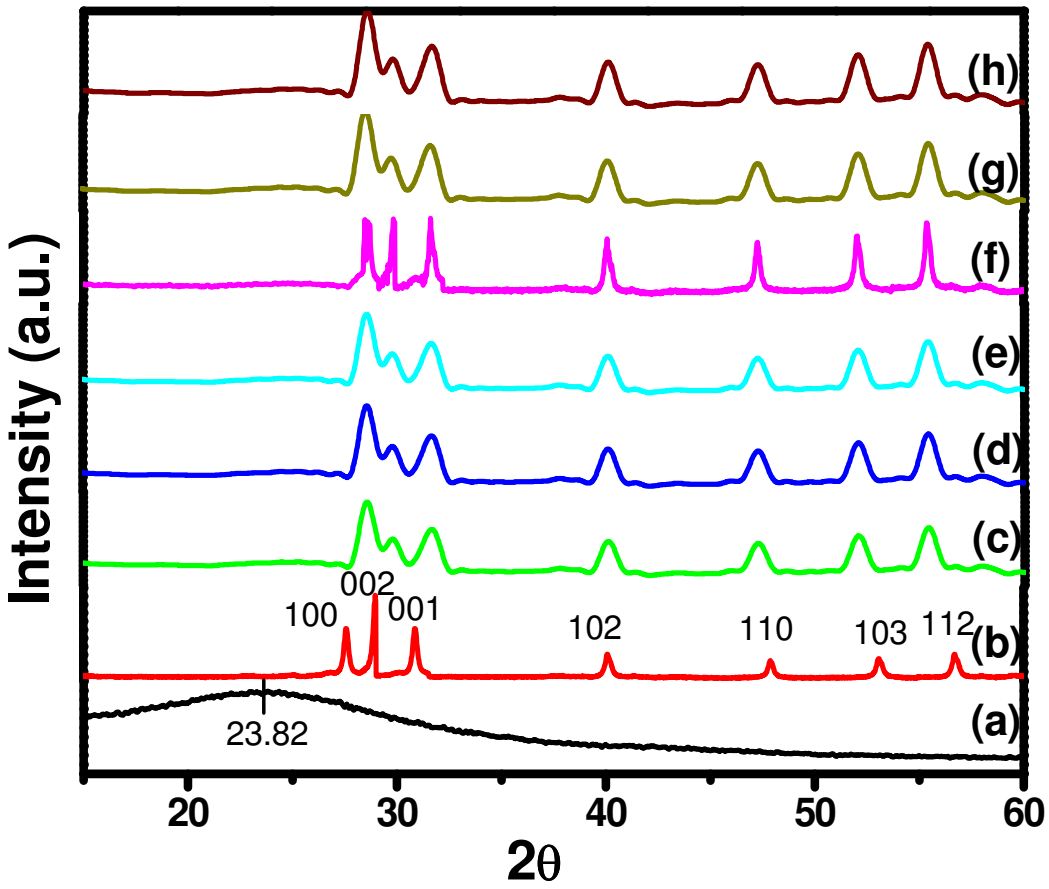

Fig. 6: WAXS spectra of (a) PANI, (b) Pure ZnS, (c) PAZ1, (d) PAZ2, (e) PAZ3, (f) PAZ4, (g) PAZ5, (h) PAZ6

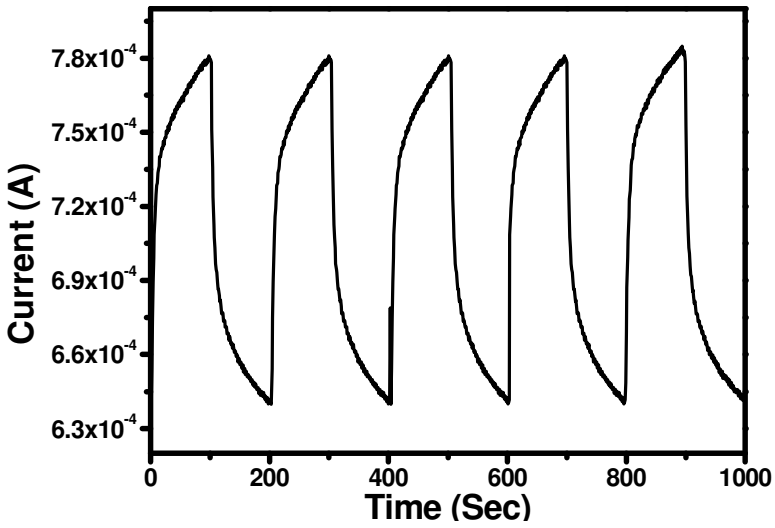

Fig. 7: Photocurrent response of the PAZ4 for different cycles

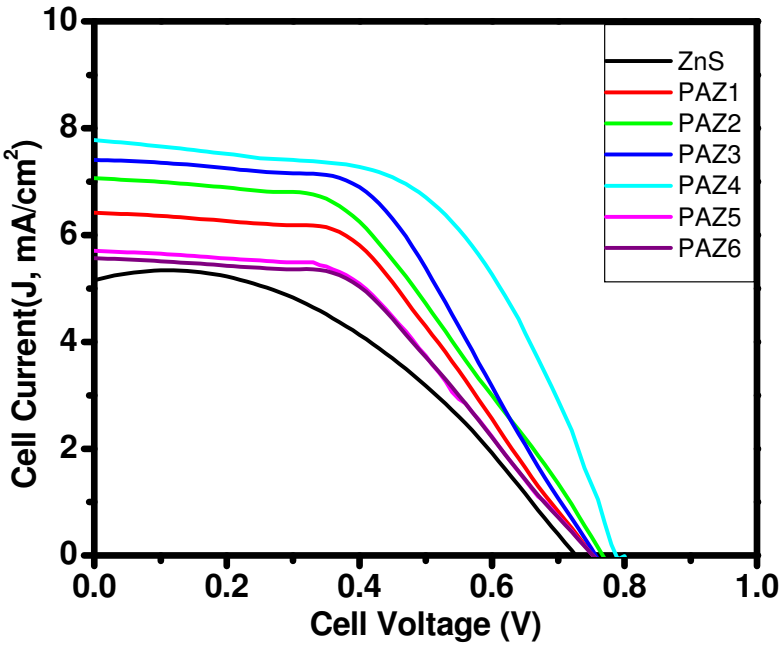

Fig. 8: J-V characteristics of Pure ZnS NPs, PAZ1, PAZ2, PAZ3, PAZ4, PAZ5 and PAZ6 under AM1.5G light illumination of 100 mW cm^{-2}

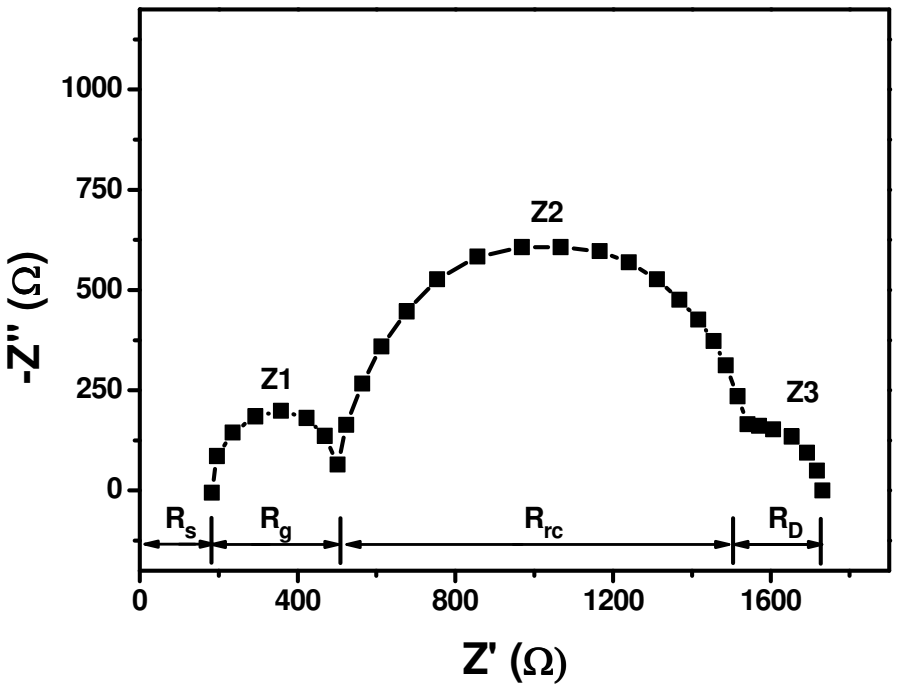

Fig. 9: Electrochemical impedance spectra of PAZ4 based DSSC

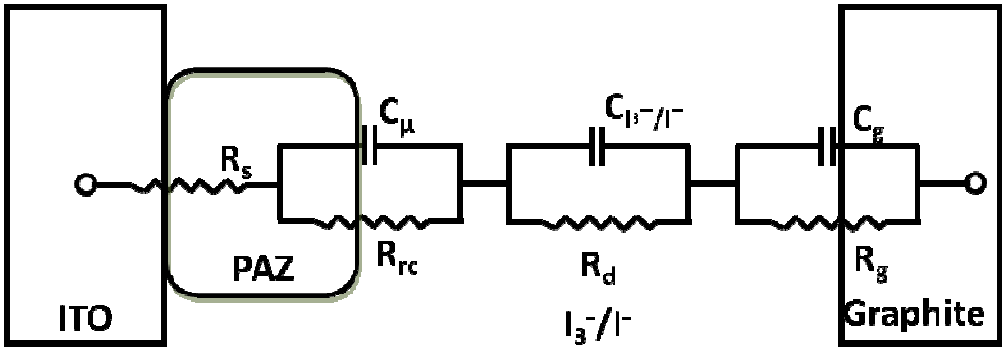

Fig. 10: Equivalent circuit diagram of impedance spectra of PAZ4 based DSSC

Table of Content

Dye Sensitized Solar Cell from Polyaniline-ZnS Nanotubes and its Characterization through Impedance Spectroscopy

Arnab Shit, Shreyam Chatterjee, and Arun K. Nandi*

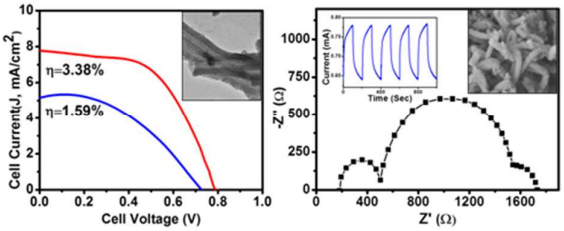

DSSC fabricated with polyaniline-ZnS nanotubes exhibits reversible turn ‘‘on’’ and ‘‘off’’with efficiency 3.4% showing nyquist plot characterizing different transport processes